

Mechanism of the Facile Nitrous Oxide fixation by Homogeneous Ruthenium Hydride Pincer Catalysts

Sílvia Escayola,[‡] Miquel Solà,^{‡,*} and Albert Poater^{‡,*}

[‡]Institut de Química Computacional i Catàlisi and Departament de Química, Universitat de Girona, C/ M^a Aurèlia Capmany 69, 17003 Girona, Catalonia, Spain

ABSTRACT: Solving ozone depletion and climate change problems require the development of effective methods for sustainably curbing them. With this aim, Milstein and coworkers developed a PNP pincer ruthenium catalyst for the homogeneous hydrogenation of nitrous oxide (N₂O), an ozone-depleting substance and the third most important greenhouse gas, to generate dinitrogen and water as resultant products. The mechanism of this promising transformation was unveiled by means of experiments together with Density Functional Theory (DFT) calculations, which inspired Milstein and coworkers to use similar (PNN)Ru-H pincer catalysts for the reduction of N₂O by CO to produce N₂ and CO₂. The use of the latter type of catalysts resulted in the proposition of a new reaction protocol and allowed to work under milder conditions. Here we describe the detailed mechanism of the last transformation catalyzed by a (PNN)Ru-H catalyst by means of DFT calculations, and not only this, but we also discover the way to block undesired parasitic reactions. Apart from that, we have explored a new evolution of this family of catalysts to go beyond previous experimental outcomes. The mechanism consists in a cascade of easy steps, starting from an insertion of the N₂O oxygen into the Ru-H bond generating a hydroxo intermediate and releasing N₂, and ending with a β -hydride elimination to form CO₂ and regenerate the catalyst. The whole process occurs in a facile way with the exception of two steps: the formation of the hydroxyl ligand and the final β -hydride elimination to form CO₂. However, the energy barriers of these two steps are not the bottleneck of the catalysis, but rather the easiness of the pyridyl group bonded to Ru to isomerize by C-H activation. We propose to solve this drawback by tuning the PNN ligand to block the pyridyl free rotation.

KEYWORDS: ruthenium, metal hydride, catalysis, pincer ligand, green chemistry, N₂O reduction, CO fixation

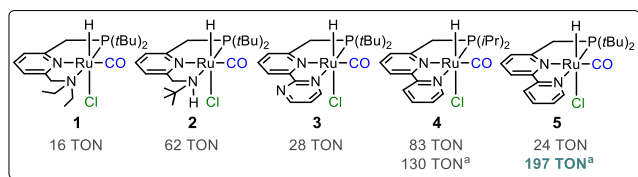
■ INTRODUCTION

Over the last fifty years, the concerns about the chemical anthropogenic perturbations to the composition of the atmosphere have become more notorious, especially because of the fatal consequences derived from it.¹ The efforts to stop and reverse this situation allowed to identify most of the global warming (GW) agents.² The variety of existing greenhouse gases (GHGs) and/or ozone depleting substances (ODSs) is huge, including gases like methane (CH₄), hydrofluorocarbons (HFCs), sulphur hexafluoride (SF₆), perfluorocarbons (PFCs), carbon dioxide (CO₂) or nitrous oxide (N₂O). Among them, CO₂ and N₂O are recognized as the main responsible agents with a great GW potential.^{3,4} By itself, CO₂ represents an 80% of the GHGs,⁵ becoming the major contributor to the GH effect, nonetheless N₂O is more harmful since it is not only a GHG but also an ODS. Whereas the traditionally dominant ODSs (chlorofluorocarbons) have been greatly reduced with the adoption of strict protocols,⁶ N₂O emissions have been maintained during the last two decades and, consequently, N₂O has become one of the today's most significant ODSs. Moreover, N₂O is nearly 300 times more powerful than CO₂ at trapping heat in the atmosphere and it is much more persistent than other GHGs such as CH₄, due to its steady-state lifetime of about 120 years.^{7,8} The main sources of N₂O are fertilizers, pesticides, and burning fossil fuels, between them agriculture is the major responsible of its generation representing a 56-81% of the anthropogenic contribution.^{9,10} Some emissions associated with food production are inevitable, and it is estimated that with a business-as-usual

scenario, by 2050 we will double our N₂O emissions.¹¹ For all these reasons, it is crucial to find ways to destruct or functionalize this hazardous gas, decreasing its levels in the atmosphere. Chemically, the cleanest way to eliminate N₂O is by a reductive process, such as the hydrogenation of N₂O to generate innocuous N₂ and H₂O. This procedure has proved feasible using homogeneous^{12,13} and heterogeneous¹⁴ catalytic systems. Thus, this sustainable reaction has become of great interest in the field of green chemistry.^{15,16} However, the reaction mechanisms of the reported homogeneous catalysts were poorly characterized, and in some cases the reactions involving N₂O and those metal complexes proceed under stoichiometric conditions.¹²

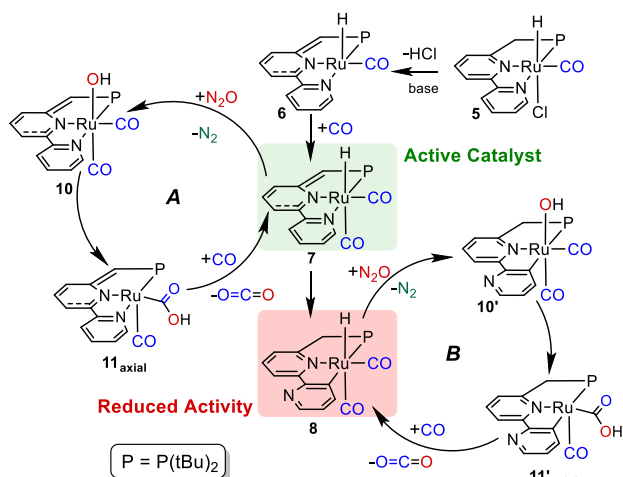
Over last years, Milstein and coworkers have been developing new metal complexes,^{13,17,18} bearing PNP and PNN pincer ligands, for the homogeneously catalyzed reduction of N₂O by H₂ and also exploring other possible reactions changing the reducing agent (*i.e.* using CO instead of H₂). The used meridional tridentate chelate ligands are prone to switch on/off the aromaticity,^{19,20} specially when being part of a pyridyl moiety affecting the reaction energetics,²¹ as Gonçalves and Huang proved from a computational point of view.²²

The new protocol for the homogeneously catalyzed N₂O reduction, with CO as reducing agent was proposed by Milstein and coworkers in 2018 using a set of ruthenium hydride pincer complexes, holding PNN pincer ligands (see Scheme 1).^{23,24} which displayed higher TONs than PNP ones.



Scheme 1. Reduction of N_2O by the PNN-pincer Ru based catalysts **1-5**. For the reaction, 0.01 mmol of catalyst, 0.01 mmol of base (*t*BuOK), 3.7 mmol of CO and 7.4 mmol of N_2O in 4 ml of toluene were used, at a temperature of 100°C during 22 h. (^a the reaction was conducted in THF at 70°C).

In the proposed reaction mechanism, the oxygen of the N_2O molecule is selectively inserted into the Ru–H bond by means of an O-atom transfer (OAT) process (first steps of cycle A in Scheme 2, from intermediate **7** to **10**). The OAT process was computationally characterized using similar Ru-based complexes,²⁵ and it is known to occur in a stepwise manner; starting with a nucleophilic attack of the hydride ligand on the N_2O terminal N followed by a concerted N_2 release.



Scheme 2. Proposed mechanism by Milstein and coworkers, with all intermediates characterized by X-Ray crystallography and/or NMR techniques.

After the OAT step, the formed Ru–OH intermediate evolves to a Ru–COOH species (intermediate **11_{axial}**, with one CO in axial position), resulting from the intramolecular nucleophilic attack of the OH moiety on the adjacent CO ligand. Next a β -hydride elimination takes place, resulting in the liberation of CO_2 and the regeneration of the catalytic species (**7**) in the presence of CO. However, the exact mechanism is still unknown. Thus, one of our goals is to characterize both the OAT and the CO_2 release steps for the particular case of the CO oxidation catalyzed by the (PNN)Ru–H complex **5** by means of Density Functional Theory (DFT). Our calculations are guided by the many experiments conducted by Milstein and coworkers²³ who gave detailed mechanistic insight

about the catalytic cycle (see Scheme 2).

Even though the (PNN)Ru–H complex presents promising catalytic activity, it is important to remark that over time the active species **7** suffers an isomerization process forming the less active for N_2O fixation compound **8**. In compound **8**, the lateral pyridine of the PNN ligand is coordinated to the metal through the C atom (in *meta* with respect the N) instead of N and the C=C double bond of the bridge connecting the phosphine ligand with the pyridine ring is reduced, resulting in the recovery of the aromaticity of the central pyridine moiety.²⁶ Consequently, we explored computationally the isomerization reaction and the catalytic cycle B to understand the decrease of the activity due to the formation of species **8**. In addition, we proposed and test new complexes with modified PNN ligands specially designed to avoid the transformation from **7** to **8**.

We also tested different Ru-based catalysts for the CO oxidation reaction, including PNP and PNN pincer ligands, to unravel the different activity according to the nature of the pincer ligand. The phosphine substituents and the solvent also influence the activity of the complex, the best candidates for the catalysis being the complexes bearing PNN ligands with $\text{P}(t\text{Bu})_2$ and $\text{P}(i\text{Pr})_2$ moieties in a THF solution.

■ RESULTS AND DISCUSSION

Calculations begin from the X-Ray data for complex **5**. Treatment of this species with a base (*t*BuOK) generates intermediate **6**. Then, the coordination of a CO ligand is exergonic by 14.5 kcal/mol and leads to the catalytically active species **7**. The catalytic cycle A in Figure 1 starts with O-atom insertion of the N_2O into the Ru–H bond with an energy barrier of 31.4 kcal/mol. The next step corresponds to the N_2 release with a barrier of 22.7 kcal/mol (33.5 kcal/mol from **7**) and extremely favored thermodynamics (62.7 kcal/mol). The kinetics are favored by 6.8 kcal/mol when assisted by an external water molecule, however without the latter assistance the energy barrier is still reasonable (29.5 kcal/mol). After the N_2 release, intermediate **10** bearing a hydroxyl ligand is rather reactive and together with the closest carbonyl ligand collapses into a carboxylic ligand *trans* to the central pyridine ring of the pincer ligand (**11_{axial}**) overcoming an energy barrier of 15.2 kcal/mol.

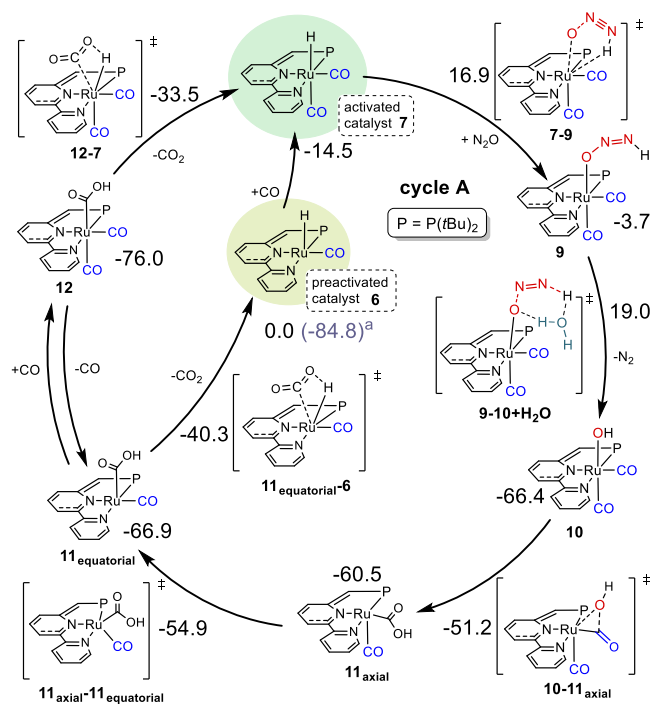


Figure 1. Computed mechanism for the CO oxidation by N_2O homogeneously catalyzed by ruthenium hydride pincer **7** following cycle A (relative Gibbs energies in solution and referred to catalyst **6**+CO+ N_2O). Energies are given in kcal/mol. All data shown were calculated at $T = 70^\circ\text{C}$, mimicking the experiments. See SI Figure S2 for a more detailed picture. ^aComplex **6** + CO_2 + N_2 after one catalytic cycle has a Gibbs energy of -84.8 kcal/mol, corresponding to the exoergonicity of the $\text{CO} + \text{N}_2\text{O} \rightarrow \text{CO}_2 + \text{N}_2$ reaction.

Due to the fact that basal sites of a nearly flat square pyramid are more π -basic than apical sites, the π -acidic ligands (*i.e.* CO) will tend to occupy these basal positions to get an extra stabilization given by the stronger backbonding.²⁷ Therefore, thermodynamics favors that the new carboxylic ligand flips to *cis* (**11_{equatorial}**), to place again a carbonyl group *trans* to the central pyridine moiety. This step is rather facile, with a low energy barrier of 5.6 kcal/mol, and releasing 6.4 kcal/mol. At this point, the final CO_2 release can follow different mechanisms starting from complex **11_{equatorial}** to regenerate the catalytic species **7** overcoming an energy barrier of 35.7 (ΔG^\ddagger between **12** and **11_{equatorial-6}**) or 42.5 kcal/mol (ΔG^\ddagger between **12** and **12-7**). In all cases, the reaction follows a stepwise process involving the coordination of a CO ligand and a β -hydride elimination to release CO_2 . The difference between them is the decooordination of the axial CO ligand. In the first case, this CO is decoordinated and then the CO_2 is released (via the transition state **11_{equatorial-6}**) forming intermediate **6**, whereas, in the other case, the CO keeps coordinated to the metal during the elimination step. The first mechanism is the most likely to occur, because the energy barrier for the second mechanism is too high to be reached working at 70°C . Moreover, even intermediate **12** is more stable than **11_{equatorial}** by 9.1 kcal/mol, the low concentration of CO in solution favors the decooordination of one CO. Therefore, the CO_2 elimination step will take place after the leaving of the labile CO

ligand, which next (after the CO_2 release) will coordinate to the ruthenium in complex **6** to recover the catalytic species **7**.

The two most kinetically demanding transition states of the catalytic cycle A correspond to the N_2 and the CO_2 releases, competing to be the rate determining step (rds). In the case of the N_2 release, there is an energy barrier of 33.5 kcal/mol even so, this step is in competition with the previous N_2O insertion, with an energy barrier of 31.4 kcal/mol, and thus, both transition states must be taken into account.²⁸ However, the absolute rds corresponds to the last CO_2 release with an energy barrier of 35.7 kcal/mol. Even though experimentally by any reason it could be possible that the CO is not able to re-coordinate from intermediate **11_{equatorial}**, it is necessary to point out that kinetically by calculations we must describe the pessimistic scenario, calculating the energy cost from **12**.

The isomer of the PNN hydride species **7**, with the aromatized PNC pincer type complex **8**, can also catalyze the CO oxidation by N_2O , as shown in Figure 2 (cycle B in Scheme 2). Qualitatively the mechanisms proceed in the same way as cycle A, in Figure 1.

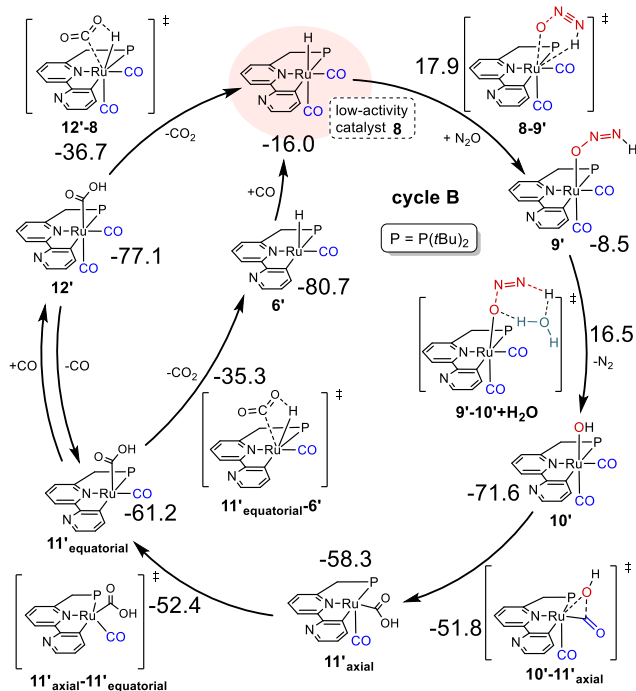


Figure 2. Computed mechanism for the CO oxidation by N_2O homogeneously catalyzed by ruthenium hydride pincer **8** following cycle B (relative Gibbs energies in solution and referred to catalyst **6**+CO+ N_2O). Energies are given in kcal/mol. All data shown were calculated at $T = 70^\circ\text{C}$, mimicking the experiments (see Figure S3 for further details).

The relative exoergonicity of **8** with respect to **7** (1.5 kcal/mol) explains in part the increase of the N_2O insertion Gibbs energy barrier by 2.5 kcal/mol. Contrarily to what happens for **7**, the N_2 release is 1.4 kcal/mol kinetically more facile than the N_2O insertion. Until the N_2O insertion step, the comparison between

PNC in cycle B and PNN pincer complex in cycle A (cycles A and B present barriers of 33.5 and 33.9 kcal/mol, respectively) suggests that cycle B is only 0.4 kcal/mol more kinetically demanding, but following with the rest of cycle B, we realize that the upper energy barrier of cycle B, *i.e.* CO₂ release, requires to overcome a barrier of 41.8 (ΔG^\ddagger between **12** and **11_{equatorial-6}**) or 40.4 (ΔG^\ddagger between **12** and **12-6**, respectively) kcal/mol. The latter energy barrier is 4.7 kcal/mol higher than for the PNN pincer type coordination (cycle A). Thus, it is also computationally confirmed, in agreement with experiments, that the PNC type coordination (cycle B) leads to a worse catalytic efficiency.

The two isomers **7** and **8** can be interconnected through the isomerization process involving the intermediates displayed in Figure 3a. We have fully characterized the whole reaction mechanism of the transformation from **7** to **8**. First of all, the decoordination of the terminal pyridine of the PNN ligand takes place with an energy barrier of 27.2 kcal/mol forming a rather unstable unsaturated intermediate (**13**). Then, if there is a proper orientation of the pyridine ring, the C-H in *meta* with respect the N

atom is activated and the intermediate **14** is formed, overcoming an energy barrier of 10.3 kcal/mol. The resulting intermediate **14** has a H₂ molecule bonded to the Ru atom. From this intermediate the system evolves to complex **8** by means of a hydrogen abstraction (inverse β -hydride elimination). As a result, we obtain species **8** overcoming an energy barrier of 10.0 kcal/mol. As a whole, the global energy barrier is of 35.9 kcal/mol starting from **7**. The resulting complex **8** is more aromatic than **7** (*vide infra*) and it is more stable too, which makes difficult the reverse step to reconvert **8** into **7**. Interestingly, the barrier that links **7** to **8** is only 0.2 kcal/mol above the upper barrier that we found for the catalytic cycle A. The small energy difference concurs with the experimental observations that the two processes occur simultaneously, resulting in less efficient catalytic activity. Moreover, by thermodynamics, with the passage of time complex **7** will be converted into **8**, which presents a less efficient mechanism (cycle B) since the reaction barrier of the rds is higher in energy than in the case of cycle A. Therefore, the detailed understanding of the conversion mechanism will help us to find out new strategies to avoid it, and thereby improving the catalysis.

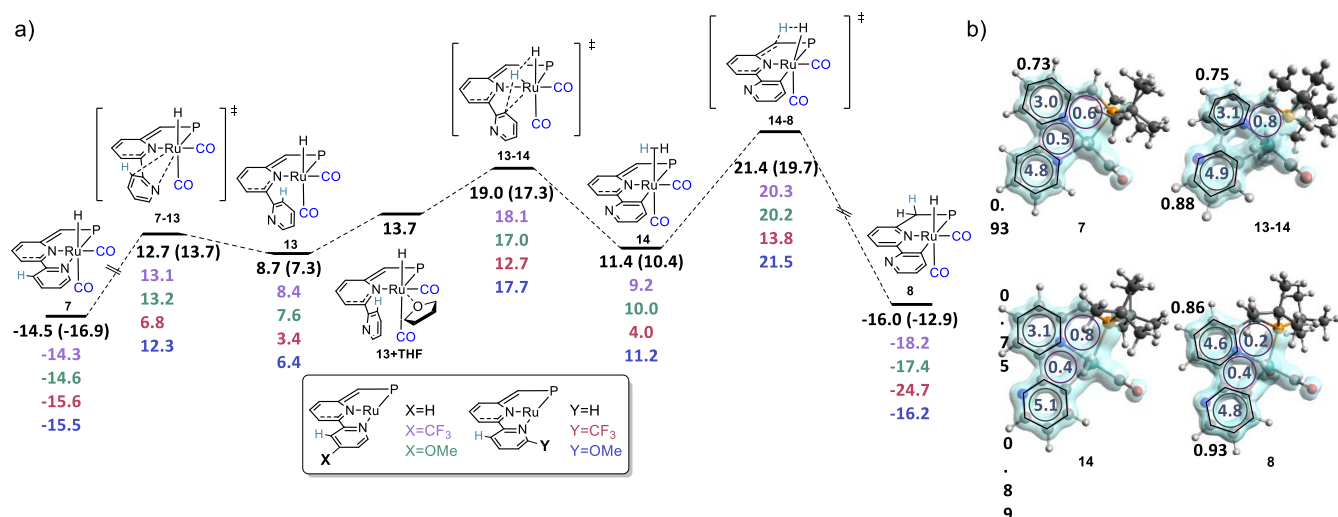


Figure 3. (a) Reaction mechanism of the interconversion between **7** and **8**, relative Gibbs energies (in kcal/mol, referred to catalyst **6**+CO+N₂O) using THF (toluene in parentheses) as solvent. In all cases and P = PtBu₂. As shown in the inset, the relative Gibbs energy values in purple, green, red, and blue correspond to the species with -CF₃ and -OMe group in *para* with respect the N (X position) or the C-H (Y position). In all cases, when X=CF₃ or OMe, Y=H and viceversa. (b) Aromaticity results: The blue surface is the global resonance (EDDB(r)_G) of the whole system and grey numbers inside the rings represent the electron density of delocalized bonds (EDDB) index for the rings of the pincer ligand, the black numbers outside the hexagons correspond to the HOMA values for the 6-MRs.

Experimentally, Milstein and coworkers found out that the catalytic activities increase when they change the solvent from toluene to tetrahydrofuran (THF). We tested the possible formation of a THF-Ru complex adduct (**13+THF**), that will block the formation of **8**. We found that the **7** THF adduct is unstable with respect to dissociation to **7** + THF by 13.7 kcal/mol, and, therefore, this intermediate is not preventing the isomerization. In addition, we computed the catalytic activity of **7** in toluene at 100°C, reproducing the experimental conditions (see Tables S2 and S4). And the barriers for N₂ and CO₂ release are 35.9 and 34.9 kcal/mol, respectively. Compared to the values obtained for THF, the N₂

release barrier has increased, becoming higher than the original β -hydride elimination rds by 0.2 kcal/mol, while for the CO₂ release it has decreased by 0.8 kcal/mol. The rds in toluene corresponds to the N₂ release, whereas in THF the rds is the CO₂ release. The former requires 0.2 kcal/mol more than the latter, in agreement with experimental observations.

To further characterize the electronic structure of compounds **7** and **8** and understand their different reactivity, we have analyzed the aromaticity, geometries, Mayer bond orders (MBO), atomic charges, and effective oxidation states (EOS) of these two species

(Figures 3b and 4 and Tables S5-S8). We employed several aromaticity indices based on magnetic, geometric, and electronic criteria, to determine the aromaticity of the two 6-membered rings (-MRs) of the pincer ligand and the two 5-MRs formed between this ligand and the metal.

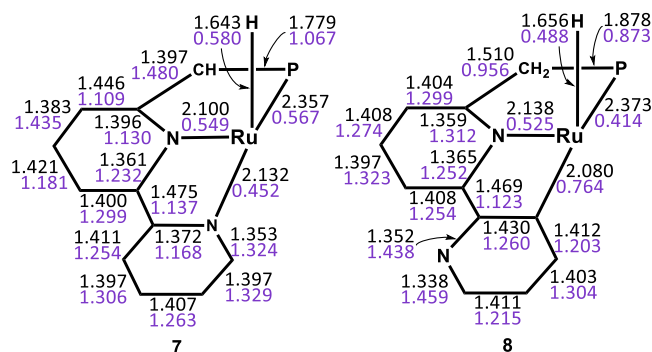


Figure 4. Bond distances in Å (black) and MBOs in e (violet) of the pincer and the hydride ligand in complexes **7** and **8**.

For the analysis of aromaticity results, we took as a reference isolated pyridine and consistently we have computed all the indices for this system. In the particular case of EDDB, isolated pyridine (our reference as aromatic compound) has a value of 5.5 delocalized electrons. For all the intermediates of the isomerization

process, the aromaticity indices employed point in the same direction, indicating that the 5-MRs are non-aromatic while the 6-MR present some aromatic character (see Figure 3b). Intermediate **8** is the most aromatic compound, with HOMA values close to 0.90 in both 6-MR. The central 6-MR of the PNN in intermediates **7**, **13-14**, and **14** (and the same for **13**, not shown in Figure 3b, but depicted in Figure S13) has weak aromatic character, with HOMA values around 0.75 and a difference of more than two delocalized electrons (with respect to pyridine) according to EDDB results. On the other hand, the external 6-MR has aromatic character in all intermediates (HOMA close to 0.90 and EDDB close to 5 electrons). Finally, in the case of intermediate **8** the central 6-MR has gained aromatic character, making both 6-MRs equally aromatic. One can also notice that part of the ~ 1.5 electrons gained by the central ring come from the C=C bond in the phosphine side, which changes its character from double (in **7**, **13**, **13-14**, and **14**) to single (in **8**) bond. The results obtained with other electronic indices (see Table S9) lead to the same conclusions.

In terms of structure, the main differences between **7** and **8** are in the central pyridine and the bridging C of the pincer. For the bridging C-C bond the distance increase by 0.113 Å from **7** to **8** and the MBO decreases by 0.524 electrons indicating that the character of the bond changes from double to single.^{2,9} On the contrary, some bonds of the central ring change the character from single (in **7**) to aromatic (in **8**), in good agreement with the aromaticity analyses.

Table 1. Gibbs energy barriers of the main elementary steps for the CO oxidation by N₂O catalyzed by ruthenium hydride complexes (shown in Figure S5 of the SI). Energies in kcal/mol for the most relevant steps of the reaction shown in Figure S6 of the SI. All data shown was calculated at T = 70°C, with THF as solvent.

catalyst	7-9	7-10+H ₂ O	9-10+H ₂ O	11 _{equatorial-6}	12-6 ^a	12-7	7-13	7-14	13-14	7-8 ^b	14-8
5	31.4	33.5	22.7	26.6	35.7	42.5	27.2	33.5	10.3	35.9	10.0
4	30.7	29.6	22.2	30.0	45.3	42.3	26.8	34.4	12.7	36.3	11.3
P(CH₃)₂	31.0	29.6	21.5	27.8	43.7	41.3	26.3	35.6	13.4	38.0	10.4
P(CF₃)₂	34.3	33.8	20.5	30.0	43.2	41.8	31.1	36.1	11.2	45.3	16.9
external o-CF₃	32.0	32.9	20.9	26.6	34.5	41.3	22.4	28.3	9.3	29.4	9.8
external p-CF₃	32.1	33.7	23.0	27.0	35.7	43.2	27.4	32.4	9.7	34.7	11.1
central p-CF₃	32.9	33.7	22.2	26.8	34.7	42.0	26.9	33.6	10.1	37.2	11.6
p-CF₃	32.5	33.8	22.8	26.4	34.4	42.5	26.8	32.3	9.8	35.9	12.7
external o-OMe	31.0	33.3	24.1	26.3	35.9	42.1	27.8	33.2	11.3	37.0	10.3
external p-OMe	31.5	33.3	23.0	26.6	35.6	42.8	27.8	31.6	9.4	34.8	10.2
central p-OMe	31.4	33.4	22.8	26.4	35.8	43.2	26.2	32.7	10.1	34.6	9.7
p-OMe	31.0	33.2	23.1	26.4	35.7	43.1	26.5	30.8	9.1	33.4	9.7
2	33.3	33.7	21.7	26.2	32.7	41.5	-	-	-	-	-
3	32.0	33.8	22.7	29.7	35.7	40.1	-	-	-	-	-
15	43.3	44.0	17.4	32.1	31.6	44.6	-	-	-	-	-
16	32.2	33.3	22.6	29.2	35.7	40.3	-	-	-	-	-

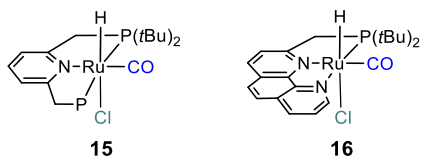
^a Non-elementary step, $\Delta G^\ddagger = G_{11\text{equatorial-6}} - G_{12}$. ^b Non-elementary step, $\Delta G^\ddagger = G_{14-8} - G_7$.

Our goal of improving the catalytic activity is focused in preventing the isomerization reaction of Figure 3. Specially, we tried to avoid the C-H activation step of this last mechanism. Further, the main steps of cycle A were also calculated for the sake of comparison between the upper barrier of the catalytic cycle with respect to the barrier of the conversion from **7** to **8**. Therefore, by means of predictive catalysis, we have proposed and tested different PNN ligands. On the one hand, we have evaluated the substituent effect

with an electron-withdrawing group (EWG, -CF₃) and an electron-donating group (EDG, -OMe) in *para* positions with respect to the N atom (**external p-X** or **external o-X**) and C-H bond (**p-X**), activated in the isomerization process, in the lateral ring of the PNN ligand (groups X and Y in Figure 3a, respectively). We also analyzed the effect of having the same EDG or EWG in *para* position with respect the N in the central ring (**central p-X**). Unfortunately, in terms of energy no significant differences were

observed, apart from a small decrease of about 1 kcal/mol in the barrier of the CO₂ release in some cases like the **external** *o*-CF₃, **central** *p*-CF₃ and *p*-CF₃. In the case of **central** *p*-CF₃, there is also an increase of more than 1 kcal/mol in the barrier of the isomerization process (barrier **7-8**, Table 1). This goes in the same direction as our aim to prevent catalyst isomerization. On the other hand, we tested the effect of changing the phosphine ligands. Going from P(*t*Bu)₂ (complex **5**) to less bulky phosphines P(*i*Pr)₂ (complex **4**), P(CH₃)₂ or P(CF₃)₂, we have seen that the **12-7** transition state becomes more kinetically facile than the **12-6** one (see Table S4) the corresponding energy barriers being 42.3, 41.3, and 41.8 kcal/mol, respectively. Anyway, in all the latter three cases, the rds is higher in energy by at least 5.7 kcal/mol than for the complex with P(*t*Bu)₂. In the case of the N₂O reduction catalysis, the substitution of the P(*t*Bu)₂ phosphine moiety by P(*i*Pr)₂ or P(CH₃)₂ improves by 3.9 and 3.8 kcal/mol, respectively, the kinetics of the first step (water assisted step **7-10+H₂O**). The reduction of the sterical hindrance on the metal center clearly facilitates the process. Thus, sterically it is possible to somewhat make up the kinetic cost. In the case of P(CF₃)₂ the energy barrier for the **7-10+H₂O** step is slightly larger by 0.3 kcal/mol than in the case of P(*t*Bu)₂. However, with all the new tested phosphines, the barrier of the last CO₂ release (either **12-6** or **12-7**) increases by at least 7.5 kcal/mol. Therefore, the change of P(*t*Bu)₂ by the less bulky P(*i*Pr)₂, P(CH₃)₂ or P(CF₃)₂ ligands does not lead to an improvement of the catalyst.

Alternatively, we have also evaluated the effect of other pincer ligands (**2**, **3**, and with another PNP ligand, **15**, see Scheme 3) previously tested experimentally by Milstein and coworkers.²³ We selected these catalysts because even though the experimental TONs obtained were lower than for **5**, their structures do not allow the isomerization of the pincer ligand (in the case of **3**, the lateral ring is a pyrimidine, thus the isomerization of the ligand gives the same compound). We found that with **2** and **3** there is no substantial difference in the energy barriers of the first two steps. However, in comparison to the reference **5**, with **15** the N₂ release process is kinetically disfavored by 10.5 kcal/mol. This is in good agreement with the fact that experimentally they just observed traces of product using **15**. Regarding the CO₂ release step, only catalyst **2** presented a smaller barrier (by 3.0 kcal/mol as compared to catalyst **5**), which is reasonable taking into account that TONs reported in toluene and 100 °C for catalysts **2** and **5** were 62 and 24, respectively. Finally, we proposed a new PNN ligand with a phenanthroline moiety (**16**) to constrain the free rotation of the lateral pyridine ring. In this case, we found similar barriers than for **5** in cycle A. Actually the N₂ release is favored by 0.2 kcal/mol, whereas the CO₂ release proceeds with the same barrier, thus the rds requires again 35.7 kcal/mol), with the advantage that the isomerization cannot take place. Consequently, we propose that **16** will be a better candidate for the catalysis.



Scheme 3. Ruthenium hydride complexes **15** and **16**.

By comparing the geometries of the transition states equivalent to **7-9** with ligands **2**, **5**, **15**, and **16**, one can notice that there is a big difference between complexes having a PNN (**2**, **5**, **16**) or PNP (**15**) ligand (Figure 5a). In the last case, the N₂O has to coordinate perpendicular to the equatorial plane due to the sterical hindrance of the *t*Bu groups of the phosphines, which explains the destabilization of this transition state. On the other hand, in case of the PNN complexes the N₂O is bent to the site of the lateral ring, minimizing the steric repulsion. Between them, these three complexes look pretty similar and it might seem that as long as we do not block the coordination site of the N₂O (by using bulky ligands) we will not increase the energy. With the transition state **11_{equatorial}-6**, the main difference comes from the possible orientation and the interaction between the O of the CO₂ with other ligands. This is the case of complex **2**, in which the structure of the transition state **11_{equatorial}-6** is stabilized by the formation of an intramolecular hydrogen bond between the O and the N-H (see **2** in Figure 5b).

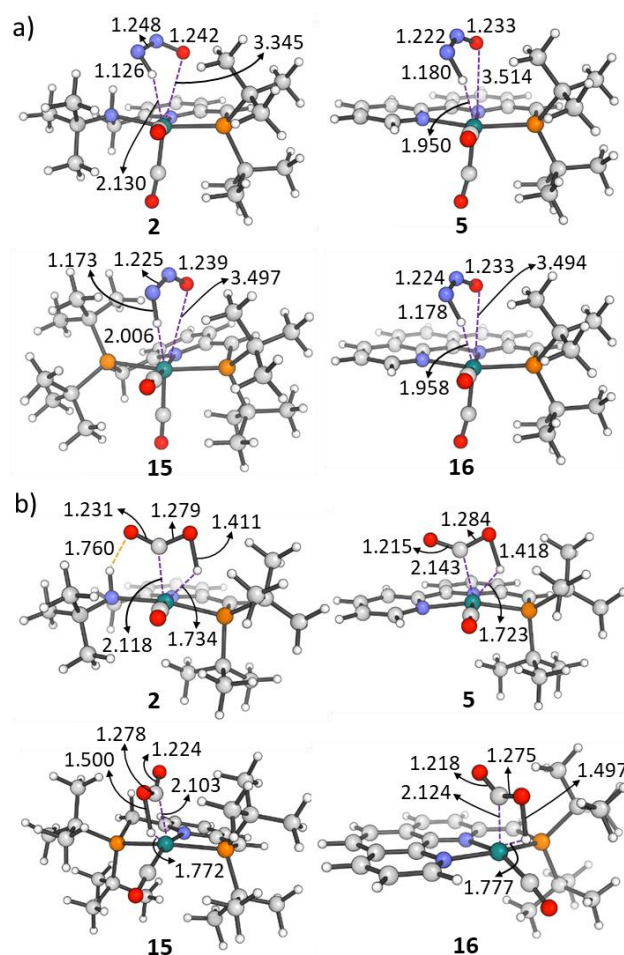


Figure 5. Transition state corresponding to steps (a) **7-9** and (b) **11_{equatorial}-6** for different catalysts (selected bond distances in Å).

■ CONCLUSIONS

Milstein and coworkers²³ developed a PNN pincer ruthenium catalyst for the homogeneous fixation of nitrous oxide (N₂O), an ozone-depleting substance and the third most important greenhouse gas, to generate dinitrogen and CO₂ as resultant products. In this work, we have performed DFT calculations to unravel the reaction mechanism. We have also analyzed different solutions to block the potential deactivation channel of the best catalyst to improve its efficiency. The characterization of the mechanism described two highly kinetically demanding steps that consist of the N₂ and CO₂ releases, being the latter the rds in THF. On the other hand, the PNN pincer ligand can isomerize to a PNC arrangement by a 180° rotation of the lateral pyridine ring, with a Ru-N bond cleavage. This isomerization reduces the catalytic performance of the catalyst. In order to address this drawback, we focused our efforts in unveiling the full mechanism of this PNC Ru based conformation, as well as the conversion from the PNN to the PNC pincer type coordination. From *in silico* predictions, we found that a phenanthroline moiety in the PNN ligand would block completely this isomerization maintaining almost identical the energy barriers of the rds of the catalytic cycle (cycle A) despite the increased rigidity of the pincer ligand.

■ COMPUTATIONAL DETAILS

All DFT static calculations were performed with the Gaussian 16 set of programs,³⁰ using the BP86 functional of Becke and Perdew,^{31,32,33} together with the Grimme D3BJ correction term to the electronic energy.³⁴ The electronic configuration of the molecular systems for main-group atoms was described with the double- ζ basis set of Ahlrichs and coworkers (standard split valence basis set with a polarization function, SVP keyword in Gaussian),³⁵ whereas for ruthenium the small-core quasi-relativistic Stuttgart/Dresden effective core potential, with an associated valence basis set (standard SDD keywords in Gaussian16), was employed.^{36,37,38} The geometry optimizations were performed without symmetry constraints, and analytical frequency calculations were carried out for the characterization of the located stationary points. These frequencies were used to calculate unscaled zero-point energies (ZPEs) as well as thermal corrections and entropy effects at 343.15 K. Energies were obtained by single-point calculations on the optimized geometries with the M06-L functional³⁹ and the cc-pVTZ basis set,⁴⁰ and estimating solvent effects with the universal solvation model SMD of Cramer and Truhlar,⁴¹ using THF as solvent. The reported Gibbs energies in this work include energies obtained at the M06-L/cc-pVTZ~sdd level of theory corrected with zero-point energies, thermal corrections, and entropy effects evaluated at 343.15 K with the BP86-D3BJ/SVP~sdd method.

In addition, we have evaluated the Mayer bond orders,⁴² 3D-space charges, effective orbitals (eff-Os), and effective oxidation states. The three later analyses, have been computed at the M06-L/cc-pVTZ~sdd/BP86-D3BJ/SVP~sdd level of theory using the topological fuzzy Voronoi cells (TFVC) 3D-space partitioning method implemented within the APOST-3D program.^{43,44} The atomic grid used for the numerical integrations was 70×434 .

The changes in local aromaticity have been quantified using electronic and structural probes of local aromaticity.⁴⁵ As electronic indices, we employed EDDB, MCI, I_{ring}, and PDI, at the M06-L/cc-pVTZ~sdd/BP86-D3BJ/SVP~sdd level of theory. The multicenter indices I_{ring}, MCI, and PDI measure the electron delocalization between different centers (just taking into account the atoms in *para* positions in the case of PDI) therefore, can be used to quantify the delocalization aspect of aromaticity.⁴⁶ In the case of EDDB, the method is based on the representation of the 1-electron density using the n-center bond orbitals, and it allows us to get visual (qualitative) and also quantitative results.⁴⁷ Finally, as a structural measure of aromaticity, the harmonic oscillator model of aromaticity (HOMA) index, defined by Kruszewski and Krygowski, was used.⁴⁸ In this case, values close to 1 are indicative of aromatic structures, while values close to 0 indicate non-aromaticity. In this case the computational level was BP86-D3BJ/SVP~sdd. The software used for the computation of all the aromaticity indices are Gaussian16 for obtaining the wavefunction files used in AIMAll together with ESI-3D packages for MCI, I_{ring}, PDI, and HOMA; and NBO 6.0 software together with the in-house code available at <http://www.eddb.pl/runeddb/> for the EDDB analysis.^{49,50,51,52}

Supporting Information

Cartesian coordinates of all studied compounds are collected in the xyz file. The extended results including: isomer benchmark, complete reaction profiles, EOS, aromaticity analysis, energies and lowest frequency in the SI pdf file. This material is available free of charge via the Internet at <http://pubs.acs.org>.

AUTHOR INFORMATION

Corresponding Author

*albert.poater@udg.edu, miquel.sola@udg.edu

ORCID

Sílvia Escayola: 0000-0002-1159-7397

Miquel Solà: 0000-0002-1917-7450

Albert Poater: 0000-0002-8997-2599

ACKNOWLEDGMENT

S.E. thanks Universitat de Girona and Donostia International Physics Center (DIPC) for an IFUdG2019 PhD fellowship. A.P. is a Serra Hünter Fellow. A.P. and M.S. thank the Ministerio de Economía y Competitividad (MINECO) of Spain for projects

PGC2018-097722-B-I00 and CTQ2017-85341-P and the Generalitat de Catalunya for project 2017SGR39 and the ICREA Academia prize 2019 awarded to A.P. We thank Prof. David Milstein for helpful discussion.

REFERENCES

- (1) Portmann, R. W.; Daniel, J. S.; Ravishankara, A. R. Research Stratospheric Ozone Depletion due to Nitrous Oxide: Influences of other Gases. *Phil. Trans. R. Soc. B* **2012**, *367*, 1256–1264.
- (2) Johnston, H. S. Reduction of Stratospheric Ozone by Nitrogen Oxide Catalysts from supersonic Transport Exhaust. *Science* **1971**, *173*, 517–522.
- (3) Freedman, B.; Frost, R. *Gale Encyclopedia of Science* **1995**, 1875–1880.
- (4) Rodhe, H. A Comparison of the Contribution of Various Greenhouse Gases to the Greenhouse Effect. *Science* **1990**, *248*, 1217–1219.
- (5) Inventory of U.S. Greenhouse Gas Emissions and Sinks: 1990–2017 (published 2019), developed by the U.S. Government to meet U.S. commitments under the United Nations Framework Convention on Climate Change (UNFCCC).
- (6) Ravishankara, A. R.; Daniel, J. S.; Portmann, R. W. Nitrous Oxide (N₂O): The Dominant Ozone-Depleting Substance Emitted in the 21st Century. *Science* **2009**, *326*, 123–125.
- (7) Hsu, J.; Prather, M. J. Global Long-Lived Chemical Modes Excited in a 3-D Chemistry Transport Model: Stratospheric N₂O, NO_x, O₃ and CH₄ Chemistry. *Geophys. Res. Lett.* **2010**, *37*, L07805.
- (8) Montzka, S. A.; Dlugokencky, E. J.; Butler, J. H. Non-CO₂ Greenhouse Gases and Climate Change. *Nature* **2011**, *476*, 43–50.
- (9) (a) Konsolakis, M. Recent Advances on Nitrous Oxide (N₂O) Decomposition over Non-Noble-Metal Oxide Catalysts: Catalytic Performance, Mechanistic Considerations, and Surface Chemistry Aspects. *ACS Catal.* **2015**, *5*, 6397–6421. (b) Severin, K. Synthetic Chemistry with Nitrous Oxide. *Chem. Soc. Rev.* **2015**, *44*, 6375–6386. (c) Parmon, V. N.; Panov, G. I.; Uriarte, A.; Noskov, A. S. Nitrous Oxide in Oxidation Chemistry and Catalysis: Application and Production. *Catal. Today* **2005**, *100*, 115–131. (d) Tolman, W. B. Binding and Activation of N₂O at Transition-Metal Centers: Recent Mechanistic Insights. *Angew. Chem., Int. Ed.* **2010**, *49*, 1018–1024.
- (10) López, J. C.; Quijano, G.; Souza, T. S. O.; Estrada, J. M.; Lebrero, R.; Muñoz, R. Biotechnologies for Greenhouse Gases (CH₄, N₂O, and CO₂) Abatement: State of the Art and Challenges. *Appl. Microbiol. Biotechnol.* **2013**, *97*, 2277–2303.
- (11) Davidson, E. A.; Kanter, D. Inventories and Scenarios of Nitrous Oxide Emissions. *Environ. Res. Lett.* **2014**, *9*, 105012–105024.
- (12) (a) Kaplan, A. W.; Bergman, R. G. Nitrous Oxide Mediated Oxygen Atom Insertion into a Ruthenium–Hydride Bond. Synthesis and Reactivity of the Monomeric Hydroxoruthenium Complex (DMPE)₂Ru(H)(OH). *Organometallics* **1997**, *16*, 1106–1108. (b) Lee, J.-H.; Pink, M.; Tomaszewski, J.; Fan, H.; Caulton, K. G. Facile Hydrogenation of N₂O by an Operationally Unsaturated Osmium Polyhydride. *J. Am. Chem. Soc.* **2007**, *129*, 8706–8707. (c) Doyle, L. E.; Piers, W. E.; Borau-Garcia, J. Ligand Cooperation in the Formal Hydrogenation of N₂O Using a PC_{sp2}P Iridium Pincer Complex. *J. Am. Chem. Soc.* **2015**, *137*, 2187–2190. (d) Gianetti, T. L.; Annen, S. P.; Santiso-Quinones, G.; Reiher, M.; Driess, M.; Grützmacher, H. Nitrous Oxide as a Hydrogen Acceptor for the Dehydrogenative Coupling of Alcohols. *Angew. Chem., Int. Ed.* **2016**, *55*, 1854–1858. (e) Gianetti, T. L.; Rodríguez-Lugo, R. E.; Harmer, J. F.; Trincado, M.; Vogt, M.; Santiso-Quinones, G.; Grützmacher, H. Zero-Valent Amino-Olefin Cobalt Complexes as Catalysts for Oxygen Atom Transfer Reactions from Nitrous Oxide. *Angew. Chem., Int. Ed.* **2016**, *55*, 15323–15328.
- (13) Zeng, R.; Feller, M.; Ben-David, Y.; Milstein, D. Hydrogenation and Hydrosilylation of Nitrous Oxide Homogeneously Catalyzed by a Metal Complex. *J. Am. Chem. Soc.* **2017**, *139*, 5720–5723.
- (14) (a) Benton, A. F.; Thacker, C. M. The Kinetics of Reaction between Nitrous Oxide and Hydrogen at a Silver Surface. *J. Am. Chem. Soc.* **1934**, *56*, 1300–1304. (b) Dixon, J. K.; Vance, J. E. The Reaction between Nitrous Oxide and Hydrogen on Platinum. *J. Am. Chem. Soc.* **1935**, *57*, 818–821. (c) Miyamoto, A.; Baba, S.; Mori, M.; Murakami, Y. Ion-Solvent Molecule Interactions in the Gas Phase. The Potassium Ion and Benzene. *J. Phys. Chem.* **1981**, *85*, 3117–3122. (d) Delahay, G.; Mauvezin, M.; Guzmán-Vargas, A.; Coq, B. Effect of the Reductant Nature on the Catalytic Removal of N₂O on Fe-Zeolite-β Catalysts. *Catal. Commun.* **2002**, *3*, 385–389. (e) Nobukawa, T.; Yoshida, M.; Okumura, K.; Tomishige, K.; Kunimori, K. Effect of Reductants in N₂O Reduction Over Fe-MFI Catalysts. *J. Catal.* **2005**, *229*, 374–388.
- (15) Chakraborty, S.; Gellrich, U.; Diskin-Posner, Y.; Leitus, G.; Avram, L.; Milstein, D. Manganese-Catalyzed N-Formylation of Amines by Methanol Liberating H₂: A Catalytic and Mechanistic Study. *Angew. Chem., Int. Ed.* **2017**, *56*, 4229–4233.
- (16) Chakraborty, S.; Kumar Das, U.; Ben-David, Y.; Milstein, D. Manganese Catalyzed α-Olefination of Nitriles by Primary Alcohols. *J. Am. Chem. Soc.* **2017**, *139*, 11710–11713.
- (17) Zhang, J.; Balaraman, E.; Leitus, G.; Milstein, D. Electron-Rich PNP- and PNN-Type Ruthenium(II) Hydrido Borohydride Pincer Complexes. Synthesis, Structure, and Catalytic Dehydrogenation of Alcohols and Hydrogenation of Esters. *Organometallics* **2011**, *30*, 5716–5724.
- (18) Zell, T.; Ben-David, Y.; Milstein, D. Highly Efficient, General Hydrogenation of Aldehydes Catalyzed by PNP Iron Pincer Complexes. *Catal. Sci. Technol.* **2015**, *5*, 822–826.
- (19) Gunanathan, C.; Milstein, D. Metal-Ligand Cooperation by Aromatization-Deaeromatization: A New Paradigm in Bond Activation and “Green” Catalysis. *Acc. Chem. Res.* **2011**, *44*, 588–602.
- (20) Luque-Urrutia, J. A.; Solà, M.; Milstein, D.; Poater, A. Mechanism of the Manganese-Pincer Catalyzed Acceptorless Dehydrogenative Coupling of Nitriles and Alcohols. *J. Am. Chem. Soc.* **2019**, *141*, 2398–2403.
- (21) (a) Kuriyama, S.; Arashiba, K.; Nakajima, K.; Tanaka, H.; Kamaru, N.; Yoshizawa, K.; Nishibayashi, Y. Catalytic Reduction of Dinitrogen to Ammonia by Use of Molybdenum–Nitride Complexes Bearing a Tridentate Triphosphine as Catalysts. *J. Am. Chem. Soc.* **2014**, *136*, 9719–9731. (b) Chang, Y.; Nakajima, Y.; Tanaka, H.; Yoshizawa, K. Facile N–H Bond Cleavage of Ammonia by an Iridium Complex Bearing a Noninnocent PNP-Pincer Type Phosphaalkene Ligand. *J. Am. Chem. Soc.* **2013**, *135*, 11791–11794. (c) Fillman, K. L.; Bielinski, E. A.; Schmeier, T. J.; Nesvet, J. C.; Woodruff, T. M.; Pan, C. J.; Takase, M. K.; Hazari, N.; Neidig, M. L. Flexible Binding of PNP Pincer Ligands to Monomeric Iron Complexes. *Inorg. Chem.* **2014**, *53*, 6066–6072. (d) Mellone, I.; Gorgas, N.; Bertini, F.; Peruzzini, M.; Kirchner, K.; Gonsalvi, L. Selective Formic Acid Dehydrogenation Catalyzed by Fe-PNP Pincer Complexes Based on the 2,6-Diaminopyridine Scaffold. *Organometallics* **2016**, *35*, 3344–3349. (e) Bailey, W. D.; Kaminsky, W.; Kemp, R. A.; Goldberg, K. I. Synthesis and Characterization of Anionic, Neutral, and Cationic PNP Pincer Pd^{II} and Pt^{II} Hydrides. *Organometallics* **2014**, *33*, 2503–2509. (f) Yang Z.; Xia, C.; Liu, D.; Liu, Y.; Sugiya, M.; Imamoto, T.; Zhang, W. P-Stereogenic PNP Pincer-Pd Catalyzed Intramolecular Hydroamination of Amino-1,3-dienes. *Org. Biomol. Chem.* **2015**, *13*, 2694–2702. (g) Cheng, C.; Kim, B. G.; Guironnet, D.; Brookhart, M.; Guan, C.; Wang, D. Y.; Krogh-Jespersen, K.; Goldman, A. S. Synthesis and Characterization of Carbazolid-Based Iridium PNP Pincer Complexes. Mechanistic and Computational Investigation of Alkene Hydrogenation: Evidence for an Ir(III)/Ir(V)/Ir(III) Catalytic Cycle. *J. Am. Chem. Soc.* **2014**, *136*, 6672–6683. (h) Alberico, E.; Lennox, A. J. J.; Vogt, L. K.; Jiao, H.; Baumann, W.; Drexler, H.; Nielsen, M.; Spannenberg, A.; Checinski, M. P.; Junge, H.; Beller, M. Unravelling

the Mechanism of Basic Aqueous Methanol Dehydrogenation Catalyzed by Ru–PNP Pincer Complexes. *J. Am. Chem. Soc.* **2016**, *138*, 14890–14904.

(i) Nakajima, Y.; Okamoto, Y.; Chang, Y. Ozawa, F. Synthesis, Structures, and Reactivity of Ruthenium Complexes with PNP-pincer Type Phosphaalkene Ligands. *Organometallics* **2013**, *32*, 2918–2925.

(j) Öztöpcü, Ö.; Holzhaacker, C.; Puchberger, M.; Weil, M.; Mereiter, K.; Veiros, L. F.; Kirchner, K. Synthesis and Characterization of Hydrido Carbonyl Molybdenum and Tungsten PNP Pincer Complexes. *Organometallics* **2013**, *32*, 3042–3052.

(k) Moha, V.; Leitner, W.; Hölscher M. H.; Synthesis in the N₂/H₂ Reaction System using Cooperative Molecular Tungsten/Rhodium Catalysis in Ionic Hydrogenation: A DFT Study. *Chem. Eur. J.* **2016**, *22*, 2624–2628.

(l) Arashiba, K.; Sasaki, K.; Kuriyama, S.; Miyake, Y.; Nakanishi, H.; Nishibayashi, Y. Synthesis and Protonation of Molybdenum- and Tungsten-Dinitrogen Complexes Bearing PNP-Type Pincer Ligands. *Organometallics* **2012**, *31*, 2035–2041.

(m) Vogt, M.; Rivada-Wheelaghan, O.; Iron, M. A.; Leitner, G.; Diskin-Posner, Y.; Shimon, L. J. W.; Ben-David, Y.; Milstein, D. Anionic Nickel(II) Complexes with Doubly Deprotonated PNP Pincer-type Ligands and Their Reactivity Toward CO₂. *Organometallics* **2013**, *32*, 300–308.

(n) Masdemont, J.; Luque-Urrutia, J. A.; Gimferrer, M.; Milstein, D.; Poater, A. Mechanism of Coupling of Alcohols and Amines to Generate Aldimines and H₂ by a Pincer Manganese Catalyst. *ACS Catal.* **2019**, *9*, 1662–1669.

(22) Gonçalves, T. P.; Huang, K.-W. Metal-Ligand Cooperative Reactivity in the (Pseudo)-Dearomatized PN₂(P) Systems: The Influence of the Zwitterionic Form in Dearomatized Pincer Complexes. *J. Am. Chem. Soc.* **2017**, *139*, 13442–13449.

(23) Zeng, R.; Feller, M.; Diskin-Posner, Y.; Shimon, L. J. W.; Ben-David, Y.; Milstein, D. CO Oxidation by N₂O Homogeneously Catalyzed by Ruthenium Hydride Pincer Complexes Indicating a New Mechanism. *J. Am. Chem. Soc.* **2018**, *140*, 7061–7064.

(24) (a) Luconi, L.; Demirci, U. B.; Peruzzini, M.; Giambastiani, G.; Rossin, A. Ammonia Borane and Hydrazine Bis(borane) Dehydrogenation Mediated by an Unsymmetrical (PNN) Ruthenium Pincer Hydride: Metal-Ligand Cooperation for Hydrogen Production. *Sustain. Energy Fuels* **2019**, *3*, 2583–2596. (b) Gusev, D. G. Revised Mechanisms of the Catalytic Alcohol Dehydrogenation and Ester Reduction with the Milstein PNN Complex of Ruthenium. *Organometallics* **2020**, *39*, 258–270.

(25) (a) Yu, H.; Jia, G.; Lin, Z. Theoretical Studies on O-Insertion Reactions of Nitrous Oxide with Ruthenium Hydride Complexes. *Organometallics* **2008**, *27*, 3825–3833. (b) Luque-Urrutia, J. A.; Poater, A. The Fundamental Noninnocent Role of Water for the Hydrogenation of Nitrous Oxide by PNP Pincer Ru-based Catalysts. *Inorg. Chem.* **2017**, *56*, 14383–14387. (c) Yao, L.; Li, Y.; Huang, L.; Guo, K.; Ren, G.; Wu, Z.; Lei, Q.; Fang, W.; Xie, H. A DFT Study on the Mechanisms of Hydrogenation and Hydrosilylation of Nitrous Oxide Catalyzed by a Ruthenium PNP Pincer Complex. *Comput. Theor. Chem.* **2018**, *1128*, 48–55. (d) Xie, H.-J.; Zhang, Y.-T.M.; Xiang, C.-Y.; Li, Y.; Fan, T.; Lei, Q.-F.; Fang, W.-J. Non-Innocent PNN Ligand is Important for CO Oxidation by N₂O Catalyzed by a (PNN)Ru–H Pincer Complex: Insights from DFT Calculations. *Dalton Trans.* **2018**, *47*, 15324–15330.

(26) Tang, S.; Von Wolff, N.; Diskin-Posner, Y.; Leitner, G.; Ben-David, Y.; Milstein, D. Pyridine-Based PCP-Ruthenium Complexes: Unusual Structures and Metal-Ligand Cooperation. *J. Am. Chem. Soc.* **2019**, *141*, 7554–7561.

(27) Rossi, A. R.; Hoffmann, R. Transition Metal Pentacoordination. *Inorg. Chem.* **1975**, *14*, 365–374.

(28) Kozuch, S.; Shaik, S. How to Conceptualize Catalytic Cycles? The Energetic Span Model. *Acc. Chem. Res.* **2011**, *44*, 101–110.

(29) (a) Magi Meconi, G.; Vummaleti, S. V. C.; Luque-Urrutia, J. A.; Belanzoni, P.; Nolan, S. P.; Jacobsen, H.; Cavallo, L.; Solà, M.; Poater, A. Mechanism of the Suzuki–Miyaura Cross-Coupling Reaction Mediated by [Pd(NHC)(allyl)Cl] Precatalysts. *Organometallics* **2017**, *36*, 2088–2095. (b) Azofra, L. M.; Poater, A. Diastereoselective Diazenyl Formation: the Key for Manganese-Catalysed Alcohol Conversion Into (E)-alkenes. *Dalton Trans.* **2019**, *48*, 14122–14127.

(30) Gaussian 16, Revision C.01, Frisch, M. J.; Trucks, G. W.; Schlegel, H. B.; Scuseria, G. E.; Robb, M. A.; Cheeseman, J. R.; Scalmani, G.; Barone, V.; Petersson, G. A.; Nakatsuji, H.; Li, X.; Caricato, M.;

Marenich, A. V.; Bloino, J.; Janesko, B. G.; Gomperts, R.; Mennucci, B.; Hratchian, H. P.; Ortiz, J. V.; Izmaylov, A. F.; Sonnenberg, J. L.; Williams-Young, D.; Ding, F.; Lipparini, F.; Egidi, F.; Goings, J.; Peng, B.; Petrone, A.; Henderson, T.; Ranasinghe, D.; Zakrzewski, V. G.; Gao, J.; Rega, N.; Zheng, G.; Liang, W.; Hada, M.; Ehara, M.; Toyota, K.; Fukuda, R.; Hasegawa, J.; Ishida, M.; Nakajima, T.; Honda, Y.; Kitao, O.; Nakai, H.; Vreven, T.; Throssell, K.; Montgomery, J. A., Jr.; Peralta, J. E.; Ogliaro, F.; Bearpark, M. J.; Heyd, J. J.; Brothers, E. N.; Kudin, K. N.; Staroverov, V. N.; Keith, T. A.; Kobayashi, R.; Normand, J.; Raghavachari, K.; Rendell, A. P.; Burant, J. C.; Iyengar, S. S.; Tomasi, J.; Cossi, M.; Millam, J. M.; Klene, M.; Adamo, C.; Cammi, R.; Ochterski, J. W.; Martin, R. L.; Morokuma, K.; Farkas, O.; Foresman, J. B.; Fox, D. J. Gaussian, Inc., Wallingford CT, 2016.

(31) Becke, A. Density-Functional Exchange-Energy Approximation with Correct Asymptotic Behaviour. *Phys. Rev. A* **1988**, *38*, 3098–3100.

(32) Perdew, J. P. Density-Functional Approximation for the Correlation Energy of the Inhomogeneous Electron Gas. *Phys. Rev. B* **1986**, *33*, 8822–8824.

(33) Perdew, J. P. Erratum: Density-functional Approximation for the Correlation Energy of the Inhomogeneous Electron Gas. *Phys. Rev. B* **1986**, *34*, 7406–7406.

(34) (a) Grimme, S.; Antony, J.; Ehrlich, S.; Krieg, H. A Consistent and Accurate Ab Initio Parametrization of Density Functional Dispersion Correction (DFT-D) for the 94 Elements H–Pu. *J. Chem. Phys.* **2010**, *132*, 154104. (b) Grimme, S.; Ehrlich, S.; Goerigk, L. Effect of the Damping Function in Dispersion Corrected Density Functional Theory. *J. Comp. Chem.* **2011**, *32*, 1456–1465.

(35) Schäfer, S.; Horn, H.; Ahlrichs, R. Fully Optimized Contracted Gaussian Basis Sets for Atoms Li to Kr. *J. Chem. Phys.* **1992**, *97*, 2571–2577.

(36) Haeusermann, U.; Dolg, M.; Stoll, H.; Preuss, H. Schwerdtfeger, P.; Pitzer, R. M. Accuracy of Energy-Adjusted Quasirelativistic Ab Initio Pseudopotentials. *Mol. Phys.* **1993**, *78*, 1211–1224.

(37) Küchle, W.; Dolg, M.; Stoll, H.; Preuss, H. Energy-Adjusted Pseudopotentials for the Actinides. Parameter Sets and Test Calculations for Thorium and Thorium Monoxide. *J. Chem. Phys.* **1994**, *100*, 7535–7542.

(38) Leininger, T.; Nicklass, A.; Stoll, H.; Dolg, M.; Schwerdtfeger, P. The Accuracy of the Pseudopotential Approximation. II. A Comparison of Various Core Sizes for Indium Pseudopotentials in Calculations for Spectroscopic Constants of InH, InF, and InCl. *J. Chem. Phys.* **1996**, *105*, 1052–1059.

(39) (a) Zhao, Y.; Truhlar, D. G. The M06 Suite of Density Functionals for Main Group Thermochemistry, Thermochemical Kinetics, Noncovalent Interactions, Excited States, and Transition Elements: Two New Functionals and Systematic Testing of Four M06-Class Functionals and 12 Other Functionals. *Theor. Chem. Acc.* **2008**, *120*, 215–241. (b) Zhao, Y.; Truhlar, D. G. A New Local Density Functional for Main-Group Thermochemistry, Transition Metal Bonding, Thermochemical Kinetics, and Noncovalent Interactions. *J. Chem. Phys.* **2006**, *125*, 194101:1–18.

(40) Kendall, R. A.; Dunning Jr., T. H.; Harrison, R. J. Electron Affinities of the First-Row Atoms Revisited. Systematic Basis Sets and Wave Functions. *J. Chem. Phys.* **1992**, *96*, 6796–6806.

(41) Marenich, A. V.; Cramer, C. J.; Truhlar, D. G. Universal Solvation Model Based on Solute Electron Density and a Continuum Model of the Solvent Defined by the Bulk Dielectric Constant and Atomic Surface Tensions. *J. Phys. Chem. B* **2009**, *113*, 6378–6396.

(42) (a) Mayer, I. Charge, Bond Order and Valence in the AB Initio SCF Theory. *Chem. Phys. Lett.* **1983**, *97*, 270–274. (b) Mayer, I. Bond Order and Valence: Relations to Mulliken's Population Analysis. *Int. J. Quantum Chem.* **1984**, *26*, 151–154.

(43) Salvador, P.; Ramos-Cordoba, E. Communication: An Approximation to Bader's Topological Atom. *J. Chem. Phys.* **2013**, *139*, 071103.

(44) (a) Ramos-Cordoba, E.; Postils, V.; Salvador, P. Oxidation States from Wave Function Analysis. *J. Chem. Theory Comput.* **2015**, *11*, 1501–1508. (b) Postils, V.; Delgado-Alonso, C.; Luis, J. M.; Salvador, P. An Objective Alternative to IUPAC's Approach To Assign Oxidation

States. *Angew. Chem., Int. Ed.* **2018**, *57*, 10525–10529. (c) Poater, J.; Gimferrer, M.; Poater, A. Covalent and Ionic Capacity of MOFs To Sorb Small Gas Molecules. *Inorg. Chem.* **2018**, *57*, 6981–6990. (d) Gimferrer, M.; Salvador, P.; Poater, A. Computational Monitoring of Oxidation States in Olefin Metathesis. *Organometallics* **2019**, *38*, 4585–4592. (e) Skara, G.; Gimferrer, M.; De Proft, F.; Salvador, P.; Pinter, B. Scrutinizing the Noninnocence of Quinone Ligands in Ruthenium Complexes: Insights from Structural, Electronic, Energy, and Effective Oxidation State Analyses. *Inorg. Chem.* **2016**, *55*, 2185–2199.

(45) (a) Poater, A.; Ribas, X.; Llobet, A.; Cavallo, L.; Solà, M. Complete Mechanism of σ^* Intramolecular Aromatic Hydroxylation through O₂ Activation by a Macrocyclic Dicopper(I) Complex. *J. Am. Chem. Soc.* **2008**, *130*, 17710–17717. (b) Poater, A.; Cavallo, L. Simple Ligand Modifications as Key to Play with the Stability of Cu(I), Cu(II) and of Cu(III)-Organometallic Complexes. *Inorg. Chem.* **2009**, *48*, 2340–2342.

(46) (a) Bultinck, P.; Ponec, R.; Van Damme, S. Multicenter Bond Indices as a New Measure of Aromaticity in Polycyclic Aromatic Hydrocarbons. *J. Phys. Org. Chem.* **2005**, *18*, 706–718. (b) Poater, J.; Fradera, X.; Duran, M.; Solà, M. The Delocalization Index as an Electronic Aromaticity Criterion: Application to a Series of Planar Polycyclic Aromatic Hydrocarbons. *Chem. Eur. J.* **2003**, *9*, 400–406. (c) Feixas, F.; Matito, E.; Poater, J.; Solà, M. Quantifying Aromaticity with Electron Delocalisation Measures. *Chem. Soc. Rev.* **2015**, *44*, 6434–6451.

(47) (a) Szczepanik, D. W.; Zak, E. J.; Dyduch, K.; Mrozek, J. Electron Delocalization Index Based on Bond Order Orbitals. *Chem. Phys. Lett.* **2014**, *593*, 154–159. (b) Szczepanik, D. W.; Andrzejak, M.; Dyduch, K.; Zak, E. J.; Makowski, M.; Mazur, G.; Mrozek, J. A Uniform Approach to the Description of Multicenter Bonding. *Phys. Chem. Chem. Phys.* **2014**, *16*, 20514–20523. (c) Szczepanik, D. W. A New Perspective on Quantifying Electron Localization and Delocalization in Molecular Systems. *Comput. Theor. Chem.* **2016**, *1080*, 33–37. (d) Szczepanik, D. W. On the Three-Center Orbital Projection Formalism Within the Electron Density of Delocalized Bonds Method. *Comput. Theor. Chem.* **2017**, *1100*, 13–17. (e) Szczepanik, D. W.; Andrzejak, M.; Dominikowska, J.; Pawełek, B.; Krygowski, T. M.; Szatyłowic, H.; Solà, M. The electron density of delocalized bonds (EDDB) applied for quantifying aromaticity. *Phys. Chem. Chem. Phys.*, **2017**, *19*, 28970–28981.

(48) Kruszewski, J.; Krygowski, T. M. Definition of Aromaticity Basing on the Harmonic Oscillator Model. *Tetrahedron Lett.* **1972**, *13*, 3839–3842.

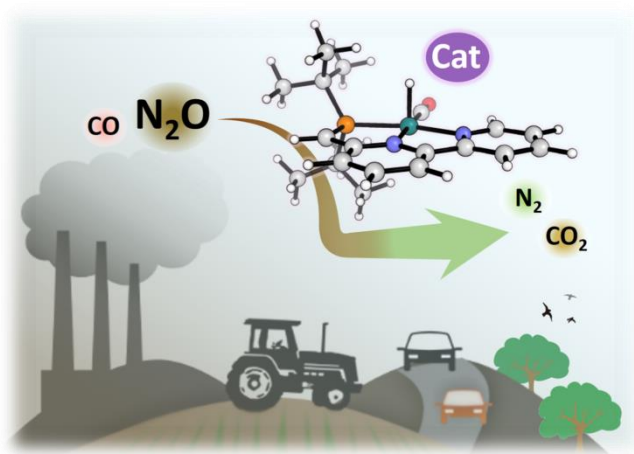
(49) Keith, T. A. AIMAll (Version 14.11.23), TK Gristmill Software: Overland Park KS, USA 2014.

(50) Matito, E. ESI-3D; IQCC and DIPIC: Donostia, Euskadi, Spain, 2015.

(51) Matito, E.; Salvador, P.; Duran, M.; Solà, M. Aromaticity Measures from Fuzzy-Atom Bond Orders (FBO). The Aromatic Fluctuation (FLU) and the para-Delocalization (PDI) Indexes. *J. Phys. Chem. A* **2006**, *110*, 5108–5113. (c) Matito, E.; Solà, M.; Salvador, P.; Duran, M. Electron Sharing Indexes at the Correlated Level. Application to Aromaticity Measures. *Faraday Discuss.* **2007**, *135*, 325–345.

(52) Glendening, E. D.; Badenhoop, J. K.; Reed, A. E.; Carpenter, J. E.; Bohmann, J. A.; Morales, C. M.; Landis, C. R.; Weinhold, F. NBO 6.0, Theoretical Chemistry Institute, University of Wisconsin: Madison, 2013.

TABLE OF CONTENTS



Better catalytic activity of a (PNN)Ru based catalyst for the reduction of N₂O by CO from DFT calculations.